Int. J. Radiation Oncology Biol. Phys., Vol. 57, No. 4, pp. 1159–1173, 2003

0360-3016/03/$–see front matter

ELSEVIER

doi:10.1016/S0630-3016(03)01564-5

PHYSICS CONTRIBUTION

QUALITY ASSURANCE OF MAGNETIC RESONANCE SPECTROSCOPIC IMAGING–DERIVED METABOLIC DATA

SANDEEP HUNJAN, PH.D.,* ELFAR ADALSTEINSSON, PH.D.,† DONG-HYUN KIM, M.SC.,† GRIFFITH R. HARSH, M.D.,* ARTHUR L. BOYER, PH.D.,* DANIEL SPIELMAN, PH.D.,* AND LEI XING, PH.D.*

*Department of Radiation Oncology and †Department of Radiology and Lucas Center for Magnetic Resonance Imaging and Spectroscopy, Stanford University School of Medicine, Stanford, CA

Purpose: Spatially resolved metabolite maps, as measured by magnetic resonance spectroscopic imaging (MRSI) methods, are being increasingly used to acquire metabolic information to guide therapy, with metabolite ratio maps perhaps providing the most diagnostic information. We present a quality assurance procedure for MRSI-derived metabolic data acquired ultimately for guiding conformal radiotherapy.

Methods and Materials: An MRSI phantom filled with brain-mimicking solutions was custom-built with an insert holding eight vials containing calibration solutions of precisely varying metabolite concentrations that emulated increasing grade/density of brain tumor. Phantom metabolite ratios calculated from fully relaxed 1D, 2D, and 3D MRS data for each vial were compared with calibrated metabolite ratios acquired at 9.4 T. Additionally, 3D ratio maps were "discretized" to eight pseudoabnormality levels on a slice-by-slice basis and the accuracy of this procedure was verified.

Results: Regression analysis revealed expected linear relationships between experimental and calibration metabolite ratios with intercepts close to zero for the three acquisition modes. 1D MRS data agreed most with theoretical considerations (regression coefficient, b = 0.969; intercept 0.008). The 2D (b = 1.049; intercept −0.199) and 3D (correlation coefficient r^2 = 0.9978–0.7336 for five slices) MRSI indicated reduced MRS data quality in regions of degraded B_0 and B_1 homogeneity. Pseudoabnormality levels were found to be consistent with expectations within regions of adequate B_0 homogeneity.

Conclusions: This simple phantom-based approach to generate baseline calibration curves for all MRS acquisition modes may be useful to identify temporal deviations from acceptable data quality in a routine clinical environment or for testing new MRS and MRSI acquisition software. © **2003 Elsevier Inc.**

Quality assurance, Phantom, MRS, MRSI.

INTRODUCTION

Recent technical advances in radiation delivery techniques, such as intensity-modulated radiotherapy (IMRT), now provide the ability to exquisitely control the three-dimensional (3D) dose delivered to tumors. The phrases "dose painting" (in two dimensions) or "dose sculpting" (in 3D) have been coined recently to describe the newly acquired capabilities to produce deliberately nonuniform dose distributions (1, 2). In this form of treatment, accurate "biologic/functional" volumetric maps showing 3D distributions of viable tumor tissue, edema, inflammation, necrosis, and normal tissue will be imperative to precisely guide the "painting" or the sculpting.

One of the most promising "biologic/functional" techniques for noninvasive monitoring of tissue activity and response to therapy is proton magnetic resonance spectroscopy (^{1}H-MRS). At a field strength of 1.5 Tesla (T) and TE 144 ms, the most commonly observed peaks in a ^{1}H-MRS correspond to choline-containing compounds (Cho: chemical shift, δ = 3.2 ppm), combined creatine and phosphocreatine (Cr) at 3.0 ppm, and *N*-acetyl aspartate (NAA) at 2.0 ppm. In addition, lactate (Lac) at 1.3 ppm is sometimes seen as an end product of anaerobic glycolysis. Intensity increase in the Cho peak is widely believed to reflect increased membrane synthesis or an increased number of cells, indicating cancer (3–6) and has been reported *in vivo* and *in vitro* in a variety of sites such as prostate (6–8),

Reprint requests to: Sandeep Hunjan, Ph.D., Department of Radiation Oncology, Stanford University School of Medicine, 300 Pasteur Drive, Stanford, CA 94305-5304. Tel: (650) 724-7620; Fax: (650) 498-4015; E-mail: shunjan@lucas.stanford.edu

Presented at the 44th Annual Meeting of the American Society of Therapeutic Radiology and Oncology, New Orleans, LA, Oct 6–10, 2002.

Supported in part by a Research Scholar Grant Award from the American Cancer Society (RSG-01-022-01-CCE), and a Research Grant from the U.S. Department of Defense, NCI 1RO1 CA98523-01.

Received Feb 24, 2003, and in revised form Jul 1, 2003. Accepted for publication Jul 7, 2003.

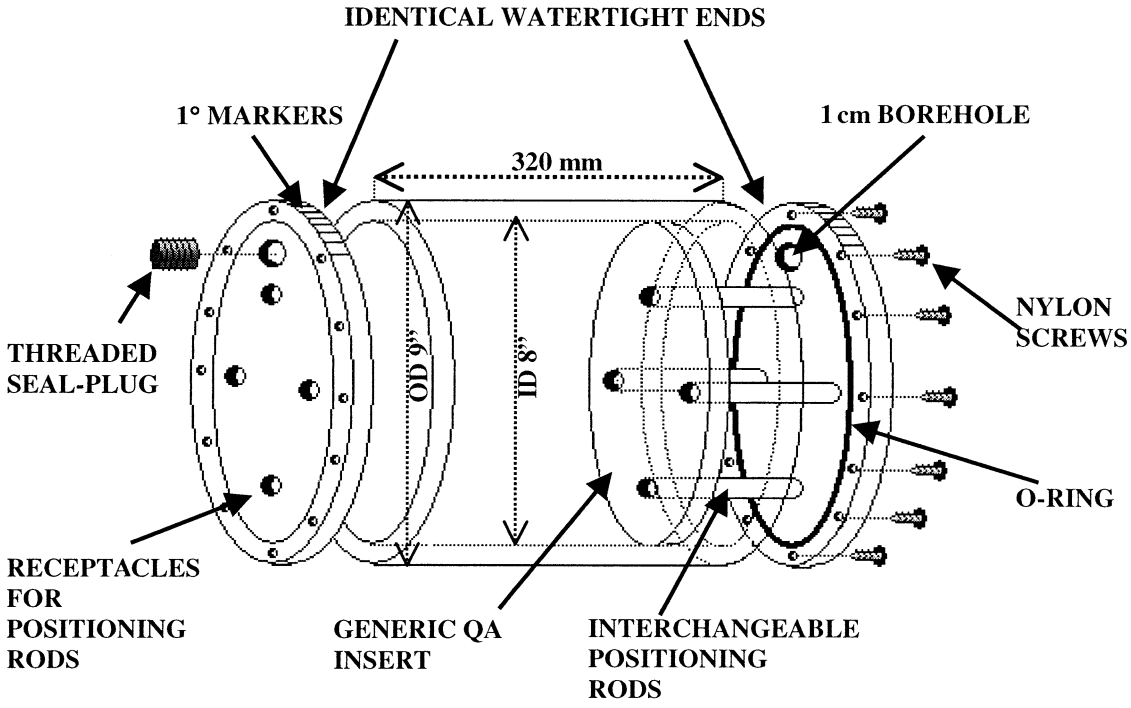

Fig. 1. Schematic illustration of the phantom body, its dimensions, and arrangement of one generic quality assurance insert via four positioning rods. Multiple inserts can be joined in a row to either end via the interchangeable rods at designated positions within the phantom. An O-ring and 12 nylon screws per lid ensure a watertight seal, whereas 1-cm-diameter threaded seal plugs allow eradication of minor bubbles.

head-and-neck (9), and breast tumors (10–12). By combining MRS with spatial localization techniques developed for magnetic resonance imaging (MRI), MRS imaging (MRSI) is possible, giving spatially localized metabolic information. Recent advances in MRSI acquisition have resulted in more accurate localization (13), faster volumetric acquisition (14), and higher spectral (15) and spatial resolution (7, 16, 17). Increasingly, neuroradiologists and neurosurgeons are using MRS to evaluate brain tumors, primarily through the observation of elevated choline and simultaneously reduced NAA, or increased Cho/NAA ratio, a robust cancer indicator in the brain (4, 5, 18–23). On the basis of the Cho/NAA ratio, investigators have been able to differentiate active tumor, normal tissue, and necrosis (18, 24–26) and demonstrate that biopsies from regions with increased Cho/NAA ratio in the brain are invariably positive for tumor (20).

To use MRSI-derived metabolic data to guide the prescription of therapeutic radiation, two major hurdles must first be overcome. The first item deals with geometric issues, such as MRSI distortion in regions of poor magnetic field homogeneity (B_0 inhomogeneity) and accuracy of data registration and fusion to primary computed tomography (CT) data sets. The second issue is the accuracy of the metabolic data. For example, metabolite peak intensities are subject to variation under imperfect B_0, rendering the measurement of spatially resolved functional information inaccurate. Both of these matters necessitate a quality assurance (QA) procedure to ensure the integrity of multimodality data acquisition, fusion, registration, transfer, and overall system functionality. In particular, we propose that there should be a QA procedure in place that addresses the need to demonstrate the accuracy of metabolite ratio measurements (e.g., Cho/NAA) and resulting quantitative indices for MRSI voxels. In this work, we introduce a magnetic resonance–compatible phantom designed specifically for multimodality quality assurance of MRI, MRSI, and CT data. We describe in detail the phantom's "metabolite ratio quantitation insert," the purpose of which is to quantitate the accuracy of metabolite ratios and resulting quantitative indices acquired using one-dimensional (1D), two-dimensional (2D), and 3D MRS and MRSI methods.

Reported in this article are the following: *(1)* the materials and methods used in the construction of the phantom and its metabolite insert; *(2)* the composition and methods of production of the phantom's filler solution and eight distinct calibration solutions for the metabolite insert; *(3)* acquisition of calibration spectra at 9.4 T plus 1D, 2D, and 3D MRS and MRSI data at 1.5 T; and *(4)* quantitation of metabolite ratio accuracy for 1D, 2D, and 3D metabolic data.

METHODS AND MATERIALS

Phantom construction

Figure 1 schematically illustrates the phantom body and arrangement of a generic QA insert via the positioning rods, together with key dimensions. The phantom's body was fabricated from cast acrylic tubing cut to 320 mm, and two watertight lids, each 228.6 mm in diameter, were con-

structed with recessed rubber O-rings to seal the ends. The resulting cylindrical phantom has removable ends, allowing easy access to the interior, which can be fitted with custom QA inserts and filled with solutions of choice. For accurate rotational positioning of the phantom in the bore of an MRI magnet, 1° markers were etched on the superior edge of the two ends. Circular Plexiglas QA inserts for testing a variety of parameters were built with a diameter slightly smaller than the internal diameter (ID) of the phantom. These were attached to four threaded, interchangeable positioning rods of customizable length, which were in turn attached to one of the lids at predetermined distances and positions inside the phantom. Multiple QA inserts could be attached to each lid via this configuration if desired. To date, several phantom QA inserts have been manufactured to test a range of CT, MRI, and MRSI parameters (27).

The metabolite ratio quantitation insert consists of eight removable, cylindrical, Plexiglas vials arranged in the configuration of a cross with a horizontal and vertical arm. The resulting array had four vials with their centers 21 mm from the axis of the phantom ("inner vials") and four vials had their centers 42 mm from the axis ("outer vials"). This allowed the testing of data quality close to, and distant from, the phantom edge where susceptibility differences between air and the phantom may perturb data quality. Each of the vials had a 28.65 mm outer diameter (OD), 21 mm ID, 21 mm cavity length, resulting in a 7.3 cc cavity volume for filling with metabolite solutions with predetermined components and concentrations. A small 1.5 mm bore hole was drilled into one end of each vial, through which calibration solutions were injected, and sealed with silicone rubber sealant. The resulting intercavity distance was also 21 mm in the horizontal and vertical directions. Figure 2a depicts a close-up of the metabolite ratio quantitation insert with calibration vials, and Fig. 2b shows the insert and vials positioned inside the sealed and filled phantom body. The central bore hole allowed rapid equilibration of phantom filler solution (described in the following section) between phantom compartments. Hence, the central area of the insert contains the filler solution during all imaging studies.

Phantom and calibration vial solutions

The phantom's brain-emulating, aqueous filler solution consisted of degassed, double deionized water with the addition of chemical species most commonly quantified in MRS studies of the brain added at room temperature in the following concentrations: 3.0 mM choline chloride, 10.0 mM creatine hydrate, 12.5 mM *N*-acetyl L-aspartic acid, and 5.0 mM DL-lactic acid (lithium salt). Respectively, these concentrations of metabolite simulate *in vivo* brain concentrations of: choline + phosphocholine + glycerophosphocholine, which constitutes the total choline peak (tCho: hereafter referred to simply as Cho) observed at 3.2 ppm; Cr at 3.0 ppm; NAA at 2 ppm; and Lac at 1.3 ppm. More importantly, for the purpose of this work, these concentrations approximate *in vivo* brain metabolite ratios when fully relaxed spectra are acquired (28–30). The exception was the Lac concentration, which, at 5.0 mM, was approximately 10-fold greater than normal brain concentrations to make detection and imaging of this metabolite possible. Table 1 summarizes these ingredients, their concentrations, and includes additional ingredients that were required for neutralizing pH, preserving the solution, and reducing relaxation times. All chemicals were obtained from Sigma-Aldrich Co. (Sigma-Aldrich Co, St. Louis, MO).

The removable calibration vials were each filled with calibration solutions 1–8, respectively, through a 1.5-mm bore hole using a syringe and sealed with silicone rubber sealant, which was cured overnight. Calibration solutions 1–8 were similar to the phantom filler solution except NAA concentrations decreased linearly from 12.5–2 mM in vials 1 through 8, respectively; Cho concentrations increased linearly from 3.0–15 mM in vials 1 through 8, respectively; and Lac concentrations increased linearly from 0–7 mM in vials 1 through 8, respectively. Table 2 summarizes the main ingredients and their concentrations for calibration solutions 1–8, which simulate hypothetical brain tumor regions with increasing tumor grade or concentrations of tumor tissue. After filling with calibration solutions and sealing, the vials were placed into their designated ports in the metabolite insert. The insert was connected to the lid via threaded positioning rods of variable lengths, screwed into four equally spaced, threaded receptacles drilled into the insert.

Acquisition of calibration metabolite ratios

Before phantom data acquisition, high-quality, fully relaxed ^{1}H-MRS were acquired from the phantom filler solution and calibration solutions 1–8 using a high-field MR spectrometer. One-dimensional proton MR spectra (1D MRS) were acquired on a Varian XL400 spectrometer operating at a field strength of 9.4 T (corresponding to a Larmor frequency of 400 MHz) equipped with a Varian console and a 5 mm probe. For each solution sample, a volume of 400 μL was pipetted into a 5-mm nuclear magnetic resonance (NMR) tube (Wilmad Glass, Buena, NJ) containing a coaxial 2-mm- diameter NMR tube insert (Wilmad) filled with D_2O (Sigma). The D_2O was required for a field-frequency lock, but was not simply added to the solution in case it perturbed relaxation times. Water suppression was achieved with selective gated irradiation at the water proton frequency via the decoupler. Proton spectra were acquired with the following parameters: spectral width (sw) = 5000 Hz, pulse width (pw) = 29 μs (90° pulse), 32 free induction decays (FIDs), acquisition time (AT) = 1.14 s, and relaxation delay = 10 s (hence, repetition time, TR = 11.14 s). In all experiments, spectra were acquired with a relaxation delay such that metabolite peaks were fully relaxed, which assured maximum signal amplitude from each peak, hence correct metabolite peak ratios. This is usually achieved by acquiring spectra with a repetition time, TR $\geq$5*T1, where T1 is the longest T1 relaxation time at the field strength of interest. NAA has the longest T1 relaxation time of the metabolites (1.41 $\pm$ 0.02 s at a field strength of

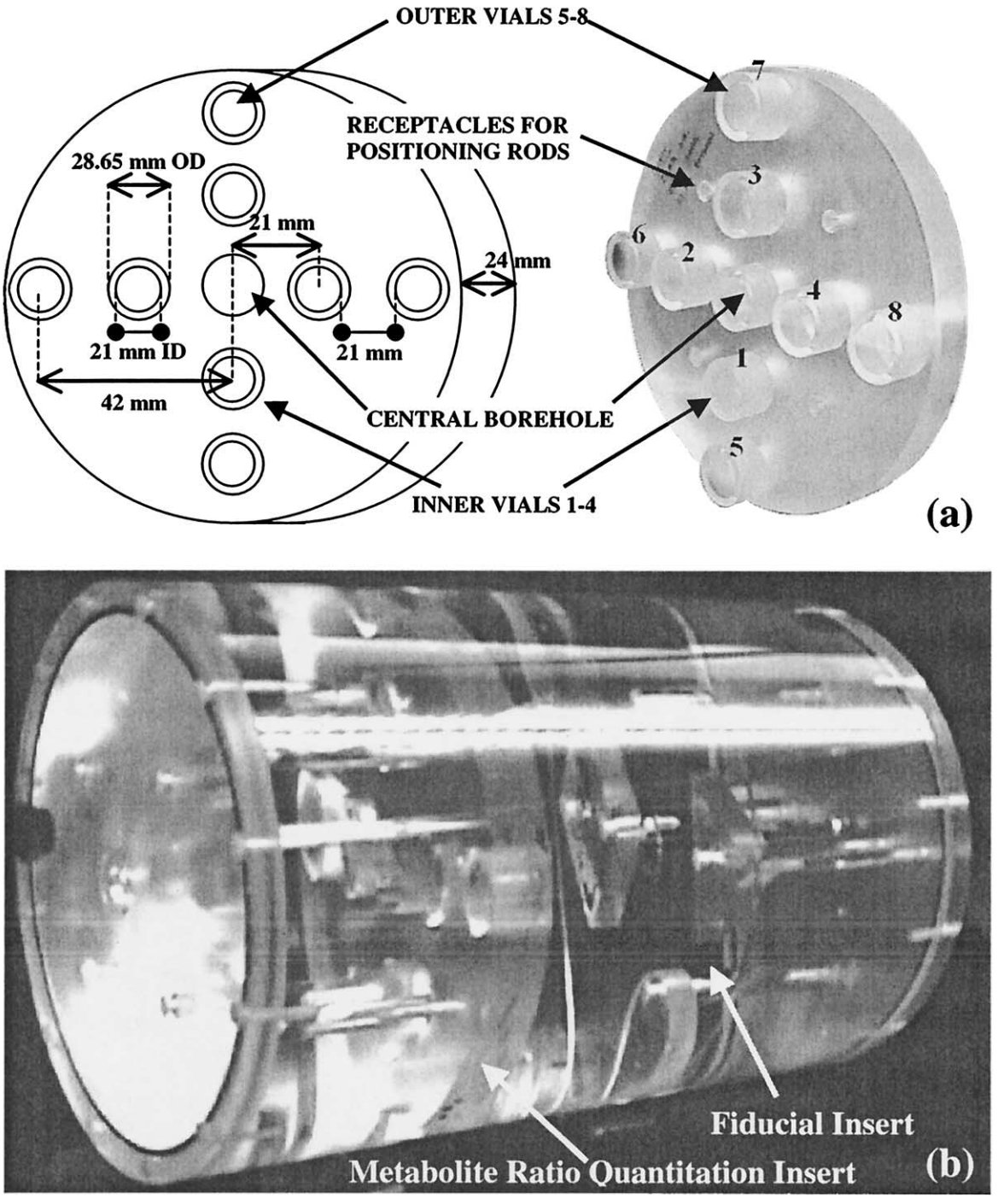

Fig. 2. (a) A closer view of the magnetic resonance spectroscopic metabolite ratio quantitation insert with calibration vials shown protruding from the body of the insert. The inner vials (in this case vials 1–4) are situated 21 mm from the central axis (CAX) and outer vials (5–8) are situated 42 mm from the CAX. The central bore hole allowed equilibration of phantom filler solution between compartments. Each vial has 28.65 mm outer diameter, 21 mm inner diameter, 21 mm cavity length, resulting in a 7.3 cc cavity volume for filling with calibration metabolite solutions. (b) The insert and vials positioned at the center of the sealed and filled cylindrical phantom body. Also visible is the fiducial insert.

9.4 T (31)), hence a relaxation delay of 10 s comfortably ensured fully relaxed spectra. The samples were spun at 20 Hz and temperature was maintained at 22°C using a thermocouple during data collection. The MR spectra of calibration solutions were processed using NUTS (ACORN-NMR, Livermore, CA) software on a personal computer running Microsoft Windows. A 3-Hz line broadening was applied to the data before Fourier transformation followed by phase correction and baseline correction. All chemical shifts were referenced to aqueous sodium 3-(trimethylsilyl)-propanesulfonate (Sigma) at 0.0 ppm. Metabolite peak integrals were measured for choline and NAA peaks using

Table 1. The ingredients, and their concentrations, for the phantom filler solution

	Chemical name	Cone (mM)
Cho	Choline chloride	3
Cre	Creatine hydrate	10
NAA	*N*-acetyl-L-aspartic acid	12.5
Lac	DL-lactic acid (lithium salt)	5
KH_2PO_4	Potassium phosphate monobasic	50
NaOH	Sodium hydroxide	56
Azide	Sodium azide	0.10%
GdDTPA	Magnevist	1 mL/L

NUTS software, and metabolite ratios were calculated for the Cho/NAA ratio for vials 1–8. These Cho/NAA metabolite ratios, acquired at 9.4 T, for vial solutions 1–8 served as the "gold standard" calibration ratios that future metabolite ratio, acquired at 1.5 T from the phantom, were evaluated against.

Phantom MRI

All subsequent phantom MRS and spectroscopic imaging data were acquired at clinical field strength of 1.5 T (Larmor frequency of 63.83 MHz) with the calibration vials placed in the MRS metabolite ratio quantitation insert, which was placed at the center of the phantom via the positioning rods. The phantom in turn was placed inside a standard GE (General Electric, Milwaukee, WI) head coil, which was positioned such that the insert would be at the center of the magnet during data acquisition. Preceding MRS, a T1-weighted axial scout scan of the phantom was acquired for the purpose of vial position evaluation with the TR/TE of 300/16 ms and a 5 mm slice thickness centered on the insert.

Single voxel MRS

Vials were subsequently evaluated with either a single voxel or multiple voxel (chemical shift imaging, CSI) MRS pulse sequence designed for optimal detection of Cho, Cre, and NAA resonances using point-resolved spectroscopy (PRESS) sequence (32). At a field strength of 1.5 T, NAA exhibits the longest T1 relaxation time of 1300–1400 ms (33). Hence, for all subsequent MR spectra acquired at 1.5 T, a TR of 7000 ms ensured fully relaxed spectra. For single voxel studies, on the basis of the scout scan, a cubic region of interest (ROI) completely enclosing each vial (approximately 8 cc) was chosen and a ^{1}H-MRS was sequentially acquired from each of the vials 1–8. For single voxel studies, shimming was performed on each ROI before data acquisition, using the vendor's built-in linear shimming procedure and water suppression was achieved using a chemical shift imaging (CHESS) sequence (34). An echo time (TE) and TR of 144 and 7000 ms, respectively, were used for single voxel studies, ensuring fully relaxed metabolite signals at 1.5 T (33); each experiment took approximately 8 min. Single voxel raw data were transferred offline for processing to a Sun SPARC station (Sun Microsystems, Palo Alto, CA) running a spectroscopic processing and display package (SAGE/IDL: GE Medical Systems) written in Interactive Data Language (Research Systems, Boulder, CO). Data were apodized with a 3-Hz Lorentzian function before Fourier transformation followed by phasing and baseline correction. Peak integrals and heights were measured for choline and NAA peaks. Integration was performed over a restricted range of frequencies for each metabolite using *a priori* knowledge of peak positions and peak widths. Fully relaxed metabolite peak area and height ratios were calculated for Cho/NAA for each of the vials 1–8. Finally, these 1D MRS Cho/NAA ratios acquired from phantom vials 1–8 were plotted on a scatter diagram against corresponding calibration ratios 1–8 acquired at 9.4 T. A regression analysis was used to investigate the relationship between the two data sets. We expected reduced data quality in outer vials because of decreasing B_0 homogeneity with increasing distance from the central axis of the phantom, toward its walls or edges. Compounding this effect, we expected random noise to negatively impact the accuracy of metabolite ratio measurements to a greater extent for vials 5–8 because NAA concentrations are decreased, hence respective MRS peaks are reduced to levels closer to the noise threshold. Therefore, this procedure was then repeated with the positions of the inner and outer vials exchanged to assess the effect of vial position on data quality.

Table 2. Summary of the concentrations of Cho, NAA, and Lac in vials 1–8*

Vial #	Cho (mM)	NAA (mM)	Lac (mM)
1	3	12.5	0
2	4.5	11	1
3	6	9.5	2
4	7.5	8	3
5	9	6.5	4
6	10.5	5	5
7	12	3.5	6
8	13.5	2	7

* The concentrations of all other chemical species remained the same as given for the filler solution (Table 1).

Abbreviations: Cho = choline-containing compounds; NAA = *N*-acetyl aspartate; Lac = lactate.

2D MRSI

Following volume-selective, single-voxel MRS studies, a 2D MRSI, or CSI, sequence was employed to interrogate the phantom inset. The quality of magnetic resonance spectroscopic imaging data is greatly affected by B_0 field homogeneity. It has previously been shown in brain studies that the use of higher order shims compared with linear terms alone yields an approximately 30% greater volume of brain tissue with adequate shim for spectroscopic imaging. In addition, regional analysis showed significant improvement in homogeneity within specific areas of the brain, particularly those near the skull (35). Therefore, for 2D MRSI, an in-house–developed shimming procedure was used that uses the scanner's first- (X,Y,Z), second- (Z (2), ZX, ZY, X (2)-Y (2), XY), and

third-order (Z (3)) shim coils. The fully automated shimming package has demonstrated robust performance in phantom and *in vivo* studies and has recently been described in detail elsewhere (36). Briefly, a spiral pulse sequence is used for rapid field map acquisition, and a regularized least-squares calculation of the shim currents is performed to minimize the root-mean-square (RMS) value of the B_0 inhomogeneity over a user-selected ROI. After shimming, and an axial scout scan to localize the calibration vials, the phantom was evaluated with a 2D PRESS (point resolved spectroscopy) MRS pulse sequence. The MRSI parameters used were as follows: TE/TR 144/7000 ms, number of excitations (NEX) = 2, field of view (FOV) 24 cm, slice thickness 15 mm, 16 × 16 array CSI grid with (1.5 cm) (3) voxels. A spectral bandwidth of 1000 Hz was used with 512 data points. Two-dimensional spectroscopic phantom data sets were transferred offline for processing with SAGE/IDL in a similar manner to single voxel phantom data. Data were apodized with a 3 Hz Lorentzian function before Fourier transformation followed by phasing and baseline correction for each voxel. The SAGE/IDL CSI package allows display of the spectra from any rectangular subarray as a stack plot. Subarrays were chosen corresponding to the positions of each vial, yielding 4–9 useful voxels per vial defined as having SNR ≥5 for the Cr peak, because the concentration of Cr is constant throughout the phantom. From each rectangular subarray, Cho and NAA peak areas and heights were measured, Cho/NAA metabolite ratios for each useful voxel per vial were calculated, and mean and standard deviation (SD) metabolite ratios were derived for each vial. These 2D MRS mean and SD Cho/NAA ratios from phantom vials 1–8 were plotted on a scatter diagram against the corresponding calibration ratios acquired at 9.4 T. A regression analysis was used to investigate the relationship between the two data sets.

3D MRSI

Next, a volumetric MRSI sequence with spiral-based k-space trajectories (14) was used to acquire 16 slices with a FOV 24 cm in *x* and *y*, and 112 mm in *z* with 64×64 pixels each slice (3.75 mm in plane resolution and 7 mm slice thickness). The spin echo (SE) volumetric MRSI sequence parameters were TE/TR = 144/7000 ms. The volumetric acquisition was preceded by a custom designed volumetric shimming procedure, as described previously (36). The shimming takes an additional 1–2 min and typically reduced the root-mean-square (rms) variation of the main field within the ROI to approximately 15 Hz. Acquisition time for metabolite data was 50 min. Reference data from the high signal-to-noise ratio (SNR) water signal were collected immediately after metabolite scans using the same sequence, except with no water suppression. The reference data, which took an additional 3 min to acquire, were required to phase metabolite data and aid in metabolite reconstruction on a voxel-by-voxel basis. A gridding algorithm (37) was applied to the raw data to resample the nonuniform, Archimedean spiral-spaced points in k-space (in k_x, k_y, k_z, k_f) onto a Cartesian grid followed by a four-dimensional fast Fourier transform (FFT) (14). After gridding and FFT, voxel-by-voxel phasing was performed on the basis of the water signal's phase. Subsequently, metabolite maps were calculated for Cho, NAA, and water by applying a frequency-domain model-based least-squares estimation for these metabolites. The amount of each metabolite was estimated for each voxel and written as 16-bit signed integer metabolite concentration maps for Cho and NAA using in-house software (14). The output data were 3D data sets with a nominal 3.5 mm thickness in *z*, interpolated from a 7 mm slice thickness resulting in 32 slices for each 3D metabolite map. Three-dimensional MRSI data were transferred for offline processing to a personal computer. A custom-designed application was used to import the 16-bit signed integer metabolite maps, calculate Cho/NAA ratios on a voxel-by-voxel basis to create the requisite metabolite ratio maps, and multiply these by a binary mask created from thresholded and binarized water images, on a slice-by-slice basis. Individual slices were exported as raw data files, which were imported into Scion Image (Scion Corporation, Frederick, MD) to measure Cho/NAA ratios for each vial. A circular ROI was first selected for each vial and measurements were made from within ROIs (on average 19 pixels per vial) of mean and SD pixel gray values, corresponding to Cho/NAA ratios. Finally, these mean and SD Cho/NAA values for calibration vials 1–8, measured using 3D MRSI techniques, were plotted on a scatter diagram against Cho/NAA ratios derived from the calibration solution spectra 1–8 at 9.4 T. Regression analysis was used to investigate the relationship between the two data sets for each slice. Volumetric MRSI acquisitions—and reduced B_0 homogeneity closer to the walls/edges of the phantom reduced B_1 amplitude resulting in less accurate tip angles may become a factor—make the reliability of metabolite quantification more difficult and a function of location. Hence, this procedure was then repeated with the positions of the inner and outer vials exchanged to assess the effect of vial position on data quality, so that vials 5–8 were placed into the "inner" ports and vials 1–4 were placed in the "outer" ports.

Metabolite quantification

To classify MRSI voxels as normal or abnormal and to standardize the procedure, an automatic, statistically determined, quantitative index is required for each voxel that determines its level of abnormality (21, 25, 26, 38). Using a simplified approach, we "discretized" a 3D volumetric ratio map to eight pseudoabnormality levels, corresponding to the expected (from calibration ratios) Cho/NAA ratios for each vial ± a 10% error. The 10% error level was arbitrarily chosen and could be set to any given value, and any method of calculating quantitative indices could equally have been investigated. The output processed data set with eight discrete pseudoabnormality levels was compared with unprocessed metabolite maps on a slice-by-slice basis to determine the number of dropped/missing voxels per vial and to examine the accuracy of abnormality level calculations.

Data processing

As described previously, Cho/NAA ratios were calculated for 1D, 2D, and 3D MRS and spectroscopic images acquired at 1.5 T for each of the vials 1–8. These values were plotted on a vial-by-vial basis on scatter diagrams against the corresponding Cho/NAA ratios 1–8 derived from calibration solution spectra at 9.4 T. Because the calibration and experimental metabolite ratios were calculated from fully relaxed spectra, theoretical considerations predicted that the functional form of the relationship between the variables in our curve would be linear, with slope 1 and intercept 0, if optimal experimental spectra, hence metabolite ratios, were acquired. If nonoptimal experimental spectra were acquired, we expected to observe quantifiable deviations from linearity in these relationships. The method of least-squares analysis was used to obtain best-fit lines for the scatter plots, regression analysis was used to investigate the linear relationships, and the coefficient of determination, r^2, was used to examine the goodness of fit and any deviations from linearity.

RESULTS

Figure 3a contains a fully relaxed, high-resolution ^{1}H-MRS acquired from the phantom filler solution at 9.4 T. Peaks A, B, C, and D, in the chemical shift range 0–3.5 ppm, correspond to the primary peaks of Cho, Cr, NAA, and Lac metabolites, respectively. The SNRs for the Cho, Cr, and NAA peaks are 1250, 1200, and 1900, respectively. The full width at half maximum (FWHM) for Cho, Cr, and NAA are 4, 3.8, and 4 Hz, respectively. The Cho/Cr, Cr/NAA, and Cho/NAA ratios are 1.12, 0.56, and 0.63, respectively. These relative heights of metabolites, hence metabolite peak ratios, are similar to those seen in the brain *in vivo* (28). The ratio of most interest to us is the Cho/NAA metabolite peak area or peak height ratio, hereafter referred to as the Cho/NAA ratio, and is examined exclusively in this work.

In addition to the MRS of the phantom filler solution, eight spectra were acquired from the eight calibration solutions (later used to fill phantom vials 1–8, respectively) at 9.4 T with the same MR parameters. The resulting spectra are displayed as a stack plot in Fig. 3b. The inset graphic shows the Cho/Cr and Cho/NAA ratios computed from these spectra for vials 1–8. Note the linearly increasing Cho/Cr ratio contrasted against the nonlinearly increasing Cho/NAA ratio. The former is due to the fact that as Cho concentration increases linearly, whereas Cr remains constant in calibration solutions 1–8. The latter is due to the simultaneous increase and decrease of Cho and NAA concentrations, respectively, for vials 1–8. The Cho/NAA ratios, derived from these calibration solution spectra acquired at 9.4 T, were used as the "gold standard" values to compare against phantom measurements of metabolite ratios at 1.5 T.

The right side of the composite Fig. 4 shows half of a T1-weighted axial scout scan of the phantom, which was acquired at 1.5 T for the purpose of vial position verification. Vial solutions can be clearly seen as well as the fluid-filled central port, whereas no signal arises from the body of the solid, circular QA insert itself. Volume-selective ROIs of approximately 8 cc were chosen such that they completely encompassed the vials, as shown in insets (c) and (d). Single voxel spectra (1D MRS) were acquired sequentially in this manner from vials 1–8 with excellent SNR ($\geq$40) and spectral resolution. The NAA peaks from inner vials (1–4) provided mean line width = 4.7 $\pm$ 0.4 Hz (range 4.3–5.2 Hz). The NAA peaks from outer vials (5–8) provided mean line width = 6.5 $\pm$ 0.7 Hz (range 6.0–7.5 Hz). These 1D spectra acquired at 1.5 T were used to calculate fully relaxed Cho/NAA metabolite peak height ratios for vials 1–8, which were compared with the "gold standard" calibration spectra Cho/NAA ratios acquired at 9.4 T by plotting the data on a scatter diagram. Although both peak height ratios and integral ratios were measured, we used peak height ratios in the 1D and 2D MRSI studies presented here because metabolite ratios based on peaks heights are less influenced by random noise (38). A second set of MRS measurements was acquired with the positions of the inner and outer vials exchanged to assess the effect of position on single voxel metabolite ratio data quality. With vials 5–8 switched to the inner positions, NAA peaks provided line widths = 4.9 $\pm$ 0.9 Hz (range 4.2–6.1). Figure 5a shows the resulting graph for the second set of data when vials 5–8 were switched to the inner positions together with a "least squares" linear fit through these data. Linear regression analysis on the data revealed a regression coefficient of 0.969, intercept 0.008, and a coefficient of determination, r^2 = 0.9993. This was in excellent agreement with theoretical considerations, which predicted that the functional form of the relationship would be linear with slope 1 and intercept 0. As a comparison, the ratios of vials 5–7 are shown superimposed on the graph, demonstrating reduced data quality when these vials were in their original positions. Subsequent to this experiment, it was found that vial 8 was not sealed and that intra- and extravial solutions had equilibrated. For this reason the data point from vial 8 has been omitted.

A similar procedure was carried out for a 2D MRSI analysis of the insert. The left side of Fig. 4 shows half of 32 $\times$ 32 PRESS array of spectra (interpolated from a 16 $\times$ 16 array) acquired from the insert. Subarrays were chosen corresponding to the positions of each vial, yielding between four and nine useful (0.75 cm) (3) voxels per vial with an SNR $\geq$5 for the Cr peak. Vial positions are indicated in the figure, and inset (a) shows a subarray positioned over inner vial 2 illustrating eight useful voxels. Inset (b) shows a subarray positioned over outer vial 5 illustrating seven useful voxels. The NAA peaks from inner vials (1–4) provided mean line width = 7.4 $\pm$ 1.1 Hz (range 6.4–8.5 Hz) and outer vial NAA peaks provided mean line width = 13.2 $\pm$ 1.6 Hz (range 11.8–15 Hz). The mean and SD Cho/NAA ratios for vials 1–8, measured using 2D MRSI techniques, are shown in Fig. 5b plotted on a scatter diagram against calibration Cho/NAA ratios 1–8 acquired at 9.4 T. In addition to producing less useful voxels per vial, the SDs of Cho/NAA ratios were significantly greater for the outer four vials,

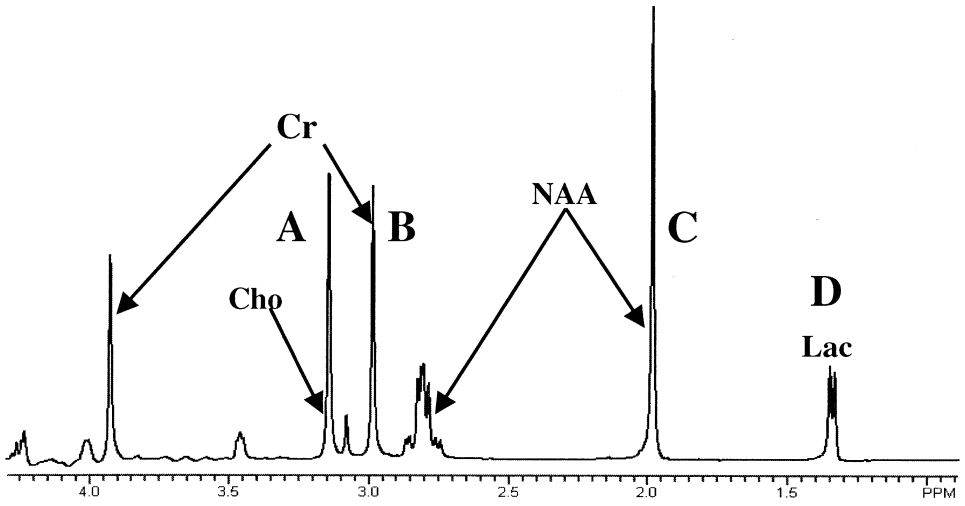

(a)

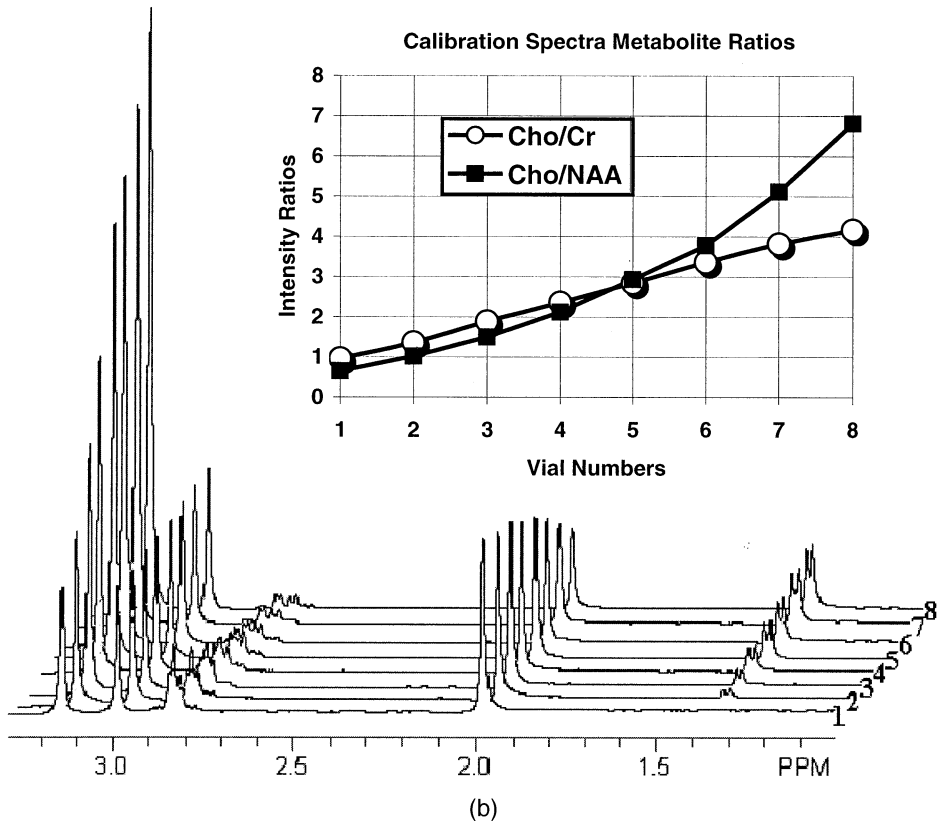

(b)

Fig. 3. (a) Fully relaxed spectrum of phantom filler solution acquired at 22°C on a 9.4 T spectrometer with TR 10s, 32 averages, and 2 Hz line-broadening. The resonance at 3.2 ppm originates from nine equivalent N-trimethyl ($(CH_3)_3$) protons of Cho, the methyl group resonance of Cr (its primary peak) is at 3.0, whereas its methylene group (secondary peak) is at 3.9 ppm, the resonance at 2.0 ppm is the primary peak of NAA, and the methyl group of Lac resonates at 1.3 ppm. (b) Stack plot showing fully relaxed spectra (repetition time = 11.14 s) from calibration vial solutions 1–8 acquired with the same parameters as the spectrum in Fig. 4. These calibration solutions were used to fill calibration vials 1–8. Note the linearly increasing Cho, decreasing NAA, and increasing Lac peak intensities. Inset shows graphic representation of the linearly increasing Cho/Cr ratio and the nonlinearly increasing Cho/NAA ratio. The latter is due to the simultaneously increasing and decreasing Cho and NAA resonances, respectively, for vials 1–8.

ranging from 0.432 to 1.343, than the inner four vials, which ranged from 0.032 to 0.127. Linear regression analysis of the data for all eight vials revealed a regression coefficient of 1.345, intercept −0.694, and a coefficient of determination, $r^2 = 0.878$. Closer examination of this relationship for the inner four vials only, depicted in

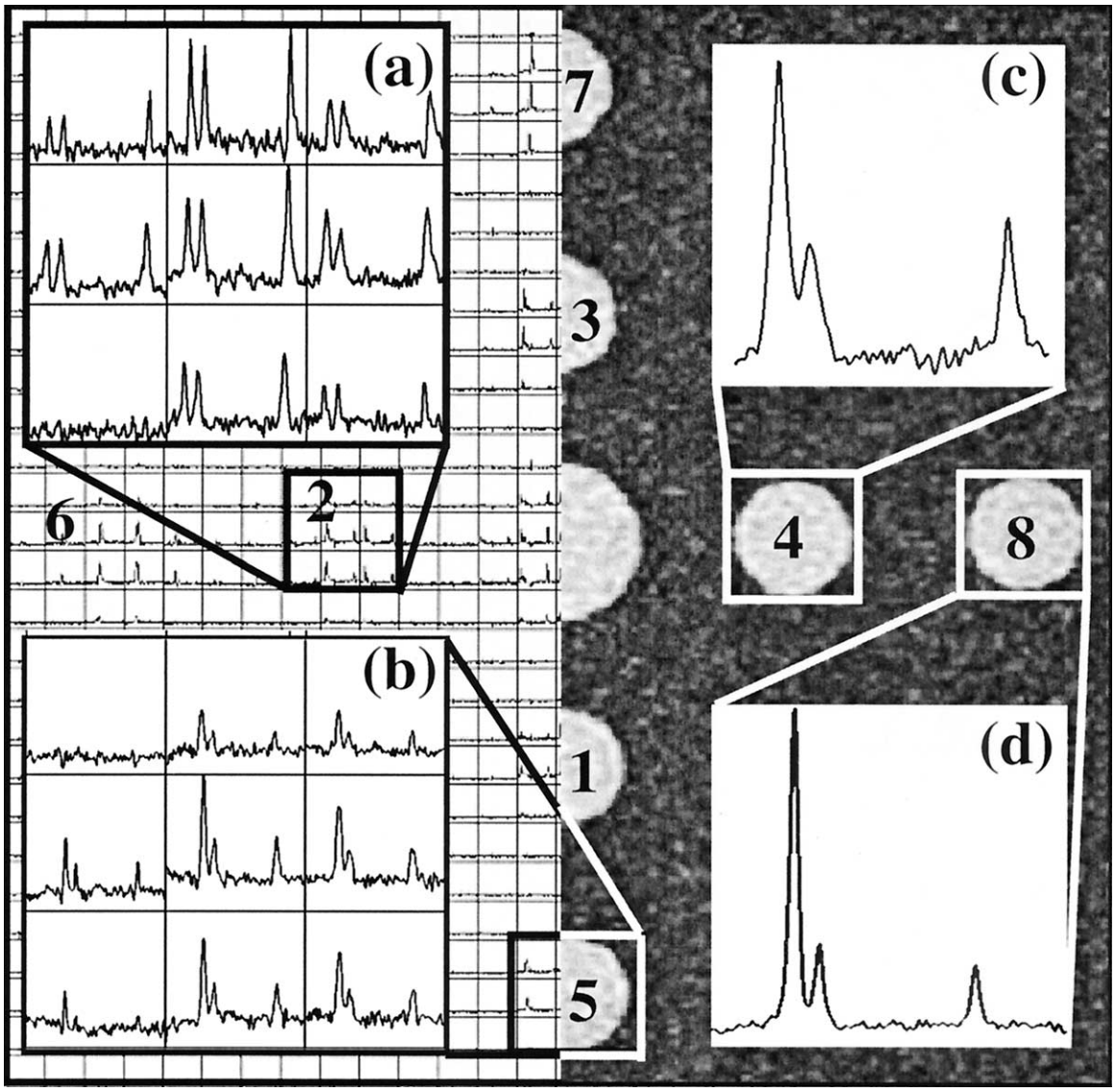

Fig. 4. A composite image showing a two-dimensional magnetic resonance spectroscopic (MR) imaging point-resolved spectroscopy scan centered on the metabolite ratio quantitation insert (left side) and an axial scout scan (right side) of the insert with signal arising from calibration vial solutions. For single voxel ^{1}H-MRS studies (1D), regions of interest of approximately 8 cc were chosen such that they completely enclosed the vials as shown for vials 4 and 8, and the resulting single voxel MR spectra are shown as insets (c) and (d), respectively. Subarrays (a) and (b) corresponding to the positions of inner and outer vials, respectively, yielded between four and nine useful voxels per vial.

Fig. 5c, revealed a regression coefficient of 1.049, intercept −0.199, and a coefficient of determination, $r^2 = 0.993$, which was much closer to the expected linear relationship with slope 1, intercept 0, and $r^2 = 1$.

Figures 6a and 6b show reconstructed and phased 3D MRSI metabolite maps displayed as "postage stamp" arrays for Cho and NAA, as well as water reference maps. Each array is composed of 32 slices (interpolated from 16) that are approximately centered on the MRS metabolite ratio quantitation insert. Slices 13 and 19 exhibit partial volume effects, with a component of the signal originating from the phantom's filler solution. Slices 14–18, however, contain signal purely from the calibration vials. These 3D MRSI metabolite maps were used to generate 3D Cho/NAA ratio maps, as illustrated in Fig. 6c, from which the mean and SD Cho/NAA values per vial were calculated on a slice-by-slice basis and plotted on scatter diagrams against corresponding calibration ratios acquired at 9.4 T. Figures 7a and 7b summarize data from slices 14 and 18, with the left side of each figure showing actual experimental ratio values compared with calibration ratios on a vial-by-vial basis, whereas the right side shows the degree of correlation between the two data sets. These results represent data acquired with vials 5–8 placed in the inner positions. From slice 14 to slice 18, a small decline in the correlation between 3D MRSI metabolite ratios and the calibration ratios is evident, with r^2 decreasing by 5% from $r^2 = 0.999$ to $r^2 = 0.949$, as shown in Fig. 7(c)(i). When vials 5–8 were in the outer

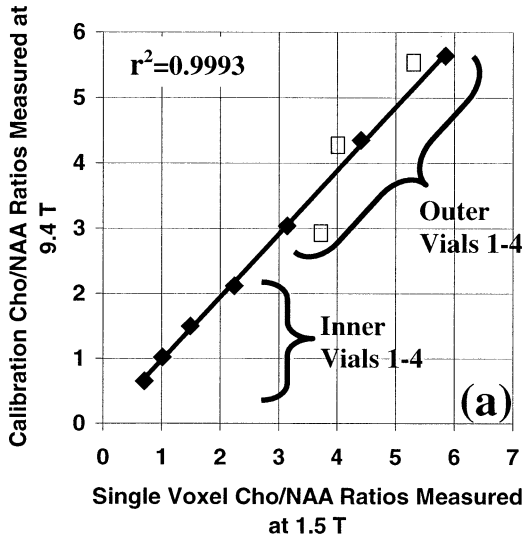

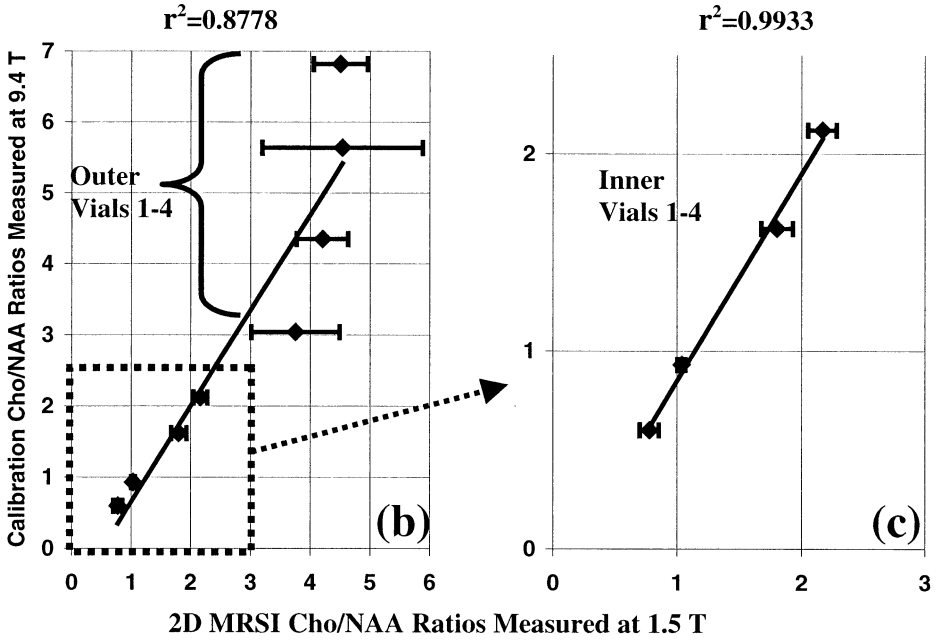

Fig. 5. The relationship between experimental metabolite ratios and calibration solution ratios obtained at 9.4 T for single voxel and two-dimensional MR spectroscopic data. (a) For single voxel spectra, solid squares indicated a linear relationship in excellent agreement with theoretical considerations between the Cho/NAA ratio vs. the calibration solution–filled vials inside the phantom obtained at 1.5 T. Superimposed open squares indicate inferior quality when vials 5–8 were in the "outer" position. (b) For a two-dimensional point-resolved spectroscopy scan sequence, there was a breakdown in linearity for the outer vials 5–8 (error bars correspond to standard deviations for 4–9 voxels per vial. (c) However, examination of inner vials only shows an improved linear relationship between experimental and calibration ratios.

positions, the value of r^2 decreased by 26.5% from $r^2 = 0.997$ to $r^2 = 0.733$ for slices 14 through 18, respectively, as shown in Fig. 7(c)(ii).

Finally, volumetric metabolite ratio maps were discretized to eight pseudoabnormality levels corresponding to the expected Cho/NAA ratios for each vial ± 10% and the accuracy of this procedure was checked. For this experiment, vials 5–8 were placed in the inner positions. Figure 6e displays the processed data for a representative slice (slice 14) shown in Fig. 6d discretized to 8 pseudoabnormality levels. Table 3 summarizes data for this slice for each vial and shows results for the number of retained voxels per vial as well as the number of incorrectly discretized voxels per vial. Each vial consisted of 17–29 voxels, with inner vials (5–8) being represented by a greater number of voxels. For this representative slice,

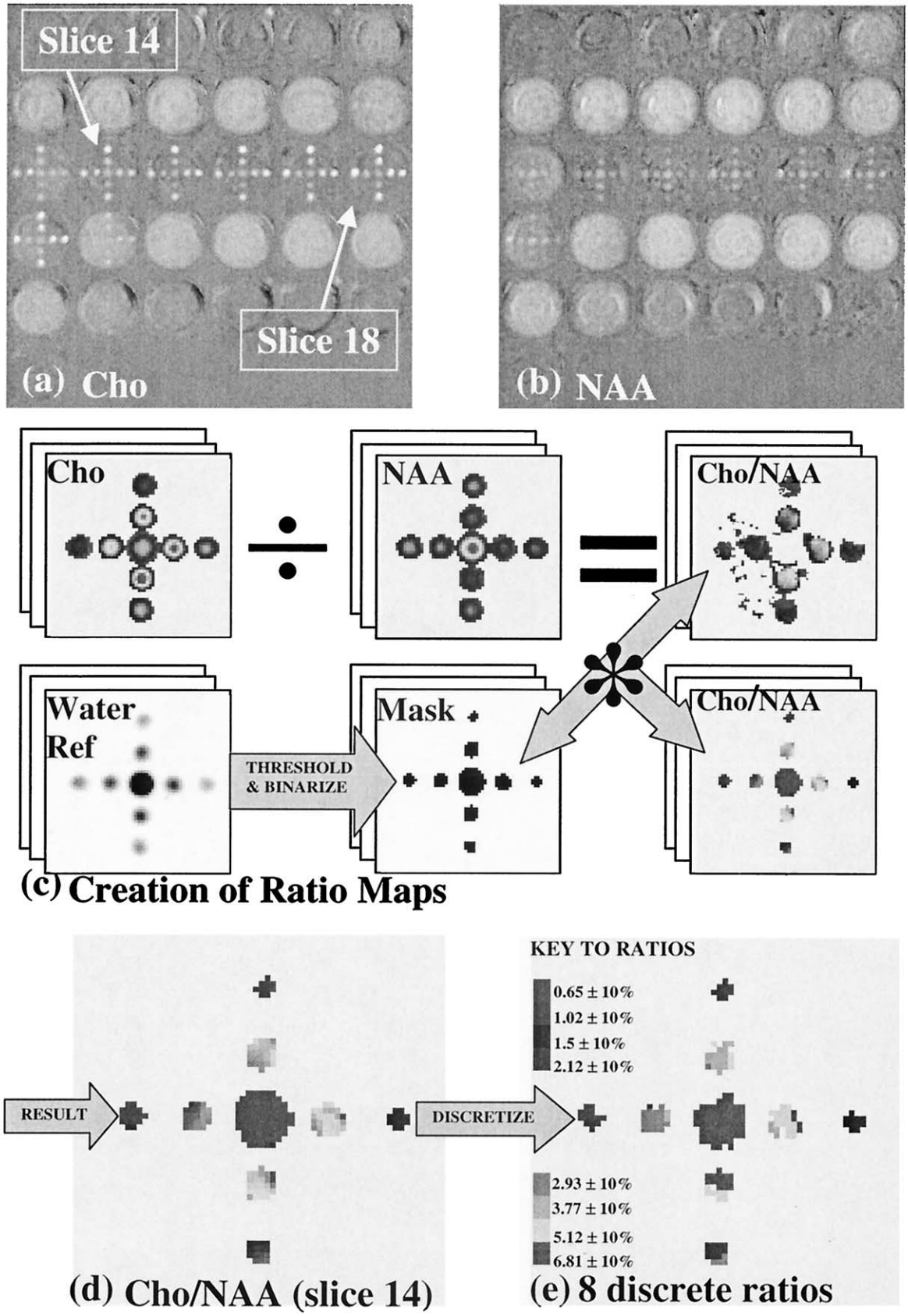

Fig. 6. (a) Three-dimensional magnetic resonance spectroscopic imaging metabolite images showing 32 slices for Cho and (b) NAA images reconstructed from phased spectra with the aid of reference water data. (c) Generation of Cho/NAA metabolite ratio map on a slice-by-slice basis. (d) A close-up of a representative slice (slice 14). (e) Eight discrete pseudoabnormality levels for slice 14 with values corresponding to expected metabolite ratios ± 10% error.

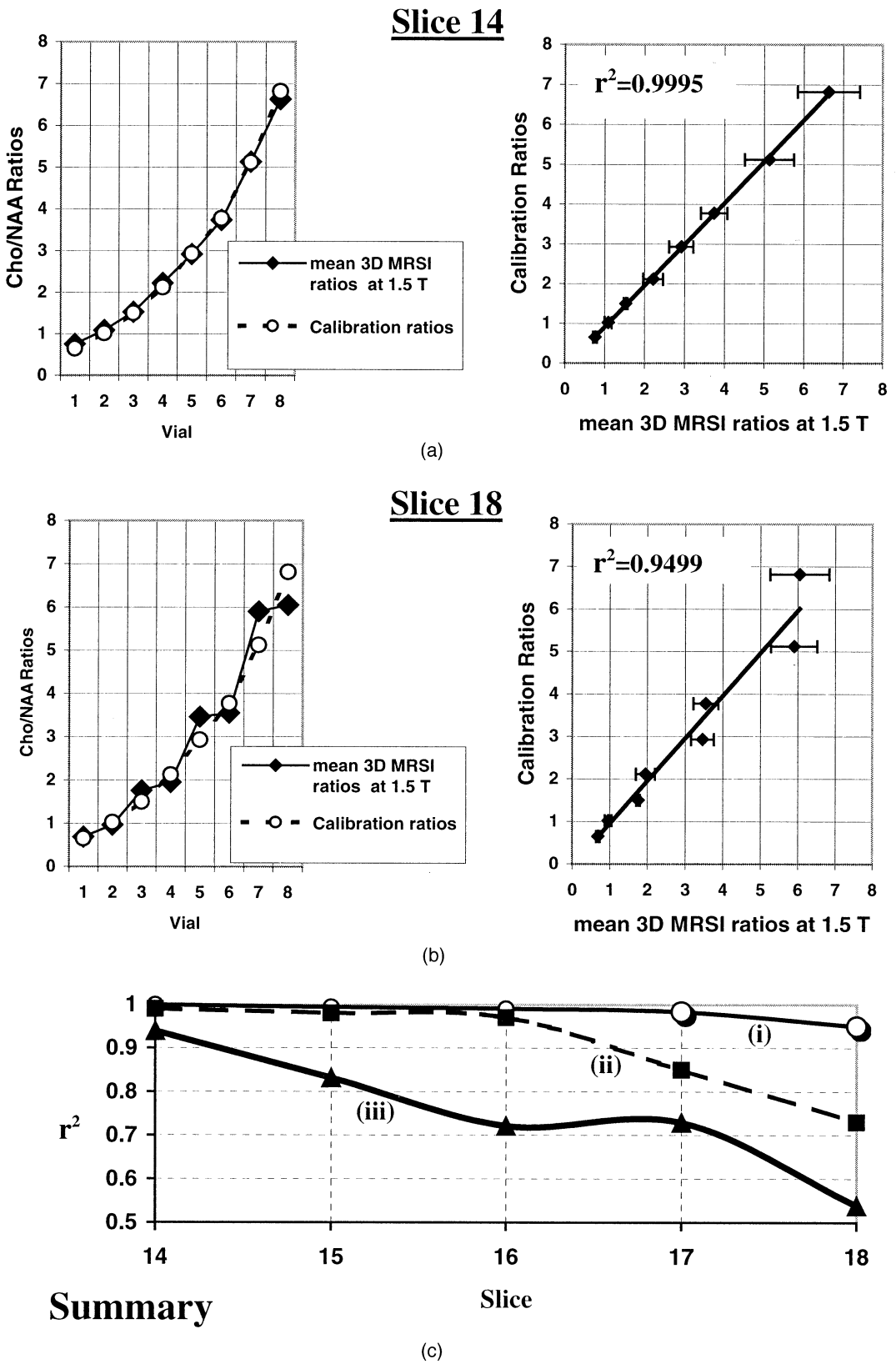

Fig. 7. Relationship between three-dimensional magnetic resonance spectroscopic imaging–derived Cho/NAA ratios vs. calibration ratios on a slice-by-slice basis. (a) and (b) summarize data from slices 14 and 18, respectively, with the left side of each figure showing actual experimental ratio values compared with calibration ratios and the right side showing the degree of correlation between the two data sets. (c)(i) A 5% decline in the r^2 from slice 14–18 compared with (c)(ii), a 26.5% decline, when vials 5–8 were in the outer positions and (c)(iii), a 43% decline, for comparable slices when the insert was placed close to the end of the phantom using shorter positioning rods.

Table 3. Results of discretization process showing the number of voxels assigned expected values, incorrect values, or no values

Vial	Initial voxels	Correctly assigned	Incorrectly assigned	Dropped
1	17	11 (65%)	4 (24%)	2 (12%)
2	10	10 (100%)	0 (0%)	0 (0%)
3	12	11 (92%)	0 (0%)	1 (8%)
4	15	11 (72%)	4 (27%)	0 (0%)
5	22	18 (82%)	3 (14%)	1 (5%)
6	25	16 (64%)	5 (20%)	4 (16%)
7	29	19 (66%)	6 (21%)	4 (14%)
8	25	15 (60%)	6 (24%)	4 (16%)

60–100% of voxels were correctly discretized to expected values for each vial, 0–27% of voxels were assigned incorrect values, and 0–16% of voxels did not meet any criteria and were "dropped" or missing in the final image. Abnormally assigned discrete values were invariably from voxels at the edge of vials.

DISCUSSION

One of the advantages that MRSI has over single voxel acquisitions (SVA) is better SNR as compared with multiple sequential SVA, because the signal from each voxel is averaged for the total collection time. The downside is that the whole volume must be first shimmed rather than each individual voxel shimmed, as in SVA, hence the shim for each CSI voxel is not as good as that on a SVA voxel in the same location. Because MRSI resolves chemical shift, B_0 inhomogeneity does not, to first order, spatially distort the images. The artifacts show up as chemical shift and broadening of peaks and, in the case of spiral-based acquisition schemes, blurring of images. Poorer shim may result in compromised solvent suppression and also image slice profiles, because slice-selective radiofrequency pulses may be less than perfect, which in turn causes problems for spectra from voxels near the outside of the CSI volume. In addition, the radiofrequency field (B_1 field) homogeneity becomes an issue near edges of the FOV, with reduced B_1 amplitude resulting in inaccurate tip angles. The resulting alterations in tip angle and phase for different voxel locations will make the reliability of metabolite quantification more difficult and a function of location. The same is true when B_0 inhomogeneity is large enough to affect the spectral passband of the excitation. Nonoptimal tip angles at the outer edges of CSI volumes also reduce SNR in these outer voxels. Thus, fewer voxels were acquired from "outer" vials for all modes of data acquisition, whether inner and outer vials were switched or not. This effect is seen in Figs. 6c and 6d, which demonstrate reduced size for the outer four vials after processing and masking the metabolite maps. In addition, because the outer vials are from edges of the CSI volume, compromised data are to be expected from these regions.

Hence, both B_1 and B_0 inhomogeneities could impact water suppression, lipid suppression, and metabolite excitation in a variety of ways depending on the acquisition strategy, but one of the advantages of the phantom is that it can be used to determine the extent to which these parameters contribute to the error in metabolite measurements. Although the phantom was designed to induce as small as possible B_0 variations resulting from air/water interfaces, the impact of poor B_0 homogeneity on measured metabolite ratios can be tested by introducing precise variations of the B_0 field, using either the gradients or nonlinear terms. Metabolite concentrations may then be measured before and after B_0 field variation in voxels within the main cylindrical body of the phantom, which contains the brain-emulating, aqueous filler solution. All of these voxels should have otherwise identical metabolite concentrations. Another method of inducing B_0 inhomogeneities in the phantom is by filling one of the calibration vials with air to simulate air-filled sinuses and measuring the resulting perturbed metabolite concentrations in proximate voxels.

The phantom extends laterally and longitudinally beyond most head sizes, so it can be used to model the impact of B_1 variations. Because B_1 homogeneity is mainly a function of the coil, to measure the effect of B_1 inhomogeneity on metabolite ratios, the B_1 field would need to be mapped while metabolite ratios are acquired with a coil exhibiting large B_1 inhomogeneities, such as a surface coil. The B_1 field maps could be used to quantitate B_1 inhomogeneity and the resultant metabolite measurements could be compared with measurements acquired under the optimum B_1 field. Metabolite concentrations could once again be measured in the filler solution or, alternatively, the calibration vials could be modified to contain identical concentrations and chemical compositions in both central as well as lateral positions to observe B_1- and B_0-induced changes in the *x* and *y* dimensions.

The curve of Fig. 5a, showing results from the single voxel spectra analysis, demonstrates improved data when the outer vials were switched with the inner vials, which placed them closer to the axis of the phantom in regions of presumably better shim. Otherwise, as the superimposed data show, data from the outer vials in their original positions were inferior. This shows evidence of B_0 homogeneity degradation in the radial direction, away from the central axis of the phantom, toward its walls/edges. In addition, random noise can be expected to degrade the data to a greater extent for vials 5–8 because NAA concentrations are decreased, hence respective MRS peaks are reduced to levels closer to the noise threshold. These effects in turn reduce the accuracy of spectroscopic data, hence metabolite ratio calculations, acquired from regions further from the central axis and/or toward the walls/edges of the phantom (i.e., vials 5–8). Further evidence for these effects comes from the 2D MRSI measurements in the phantom as seen in Figs. 5b and 5c in which the standard deviation of values from the outer vials degrades the linear relationship that would

otherwise exist between calibration and experimentally measured metabolite ratios. For these reasons, it was deemed wise to switch the inner and outer vials for several of the studies presented here and to use peak height ratios that are known to be less influential by random noise than peak integral ratios (38).

Even with optimal shimming, *in vivo* spectra are often degraded when ROIs are chosen that are close to regions of susceptibility that differ significantly from that of soft tissue, such as closed air–filled sinus cavities; this problem is worse where the air-tissue interface is orthogonal to the B_0 direction. For 3D MRSI data summarized in Fig. 7(c)(ii), the value of r^2 decreased by 26.5% from $r^2 = 0.997$ to $r^2 = 0.733$ for slices 14 through 18, respectively. We postulate that this is once again the result of decreasing magnetic field homogeneity—in this case, in the longitudinal direction along the axis of the cylindrical phantom—toward either end where the air-water interface is orthogonal to the B_0 direction. This in turn reduces the quality of spectroscopic data, hence metabolite ratio calculations, acquired from regions further from the center along the central axis, toward either end of the phantom (e.g., slice 18 as compared with slice 14). In a previous 3D MRSI experiment, the insert was placed closer to the end of the phantom using shorter positioning rods. The resulting ratios were degraded to a greater extent than were the present data because of proximity to the air-water interface at the end of the phantom, as summarized by curve (iii) in Fig. 7c.

Automatic classification of the abnormality level of MRSI voxels has been endorsed (21, 25, 26, 38) as a standardized means to determine a quantitative index for each voxel. However, to date, investigators have only had homogeneous, fluid-filled phantoms to investigate the accuracy of automatically generated quantitative indices based on metabolite ratios. We propose that there should be a rigorous QA procedure in place that demonstrates that the accuracy of quantitative indices for MRSI voxels is within tolerance levels for guiding therapy, such as MRSI-guided 3D conformal radiation therapy. In addition, after creating baseline accuracy levels, this accuracy should be checked on a routine basis using such procedures as we have outlined here to preclude degradation in the MRS system. Using a simplified approach, we "discretized" a 3D volumetric ratio map to eight pseudoabnormality levels simply by corresponding the expected Cho/NAA ratios for each vial plus or minus a 10% error. The power of this method is that, because the exact metabolite ratios for every phantom vial are known *a priori*, any automatically generated statistical measure of abnormality can be checked for its precision and accuracy under optimum conditions in a phantom. For simplicity and for visual effect, we chose our pseudoabnormality levels to match the known ratios of vials 1–8 and then investigated the number of correctly assigned, incorrectly assigned, and "dropped" voxels. The level of acceptable error can be chosen in advance and the MRS system's quality can be checked for 1D, 2D, or 3D acquisition modes on a routine basis.

To avoid the problem of degraded spectra in the outer positions, future inserts could be designed with all vials placed as close as possible to, and equidistant from, the central axis of the phantom. However, the phantom in its current configuration provides valuable information for investigators about data quality close to the edge of the CSI box. It is for this reason that the phantom was specifically designed with vials placed at two different distances from the central axis. The insert could also be placed directly at the center of the phantom to reduce the "edge effects" observed in slices from 3D data proximal to the ends.

We chose to calculate metabolite maps for Cho and NAA to quantitate the accuracy of the Cho/NAA ratio, which is the most commonly used metabolite ratio in the brain. However, we can also automatically generate equivalent metabolite maps for Cr and Lac (14) and hence other metabolite ratio maps such as Cho/Cr. Several brain metabolites such as glutamine and myoinositol were omitted to simplify spectra. These could easily be added in the appropriate concentrations for investigators interested in these metabolites. However, the lack of additional metabolite, lipid, and macromolecule signals leads to simplified, well-resolved spectra with flat baselines, which aids in the detection of problems associated with data acquisition or processing, hence facilitating an effective QA procedure. Moreover, the phantom can easily be converted to emulate organs other than the brain. For example, using solutions containing predetermined concentration of Cho, Cr, and citrate, the phantom and vials can be used to investigate issues pertinent to MRS investigations of the normal and diseased prostate gland.

CONCLUSION

Metabolic and functional imaging methods will increasingly be used clinically to define the spatial extent of many tumors. Among many issues, one of the most important is to ensure the accuracy of the obtained metabolic information. In the case of MRSI, one of the most promising of these techniques, the accuracy of measured metabolite intensities and resulting voxel quantitative indices must be ensured. In this work, we have described the design of a QA phantom and outlined the procedure for analyzing the precision of MRSI-derived metabolic information. The procedure was tested on 1D, 2D, and 3D MRS data acquired on a clinical MR scanner. The QA procedure was simple to implement on a clinical scanner and produced baseline calibration curves for 1D, 2D, and 3D MRS and MRSI data sets. In addition, this method allows MR spectroscopists to check the quality of any type of quantitative voxel indices derived from MRSI data. These parameters can be acquired on a routine basis for busy MR scanners, which should allow deviations from acceptable limits to be identified early. This article describes the first attempt to create a procedure for rigorous QA testing of MRS and MRSI metabolite data quality. This QA procedure is easy to reproduce for MR physicists and spectroscopists and can be performed on a regular basis such as annually or as part of the commissioning of a new scanner or software/pulse-sequence update.

REFERENCES

1. Ling CC, Humm J, Larson S, *et al.* Towards multidimensional radiotherapy (MD-CRT): Biological imaging and biological conformality [see comments]. *Int J Radiat Oncol Biol Phys* 2000;47:551–560.
2. Xing L, Cotrutz C, Hunjan S, *et al.* Inverse planning for functional image guided intensity modulated radiation therapy. *Phys Med Biol* 2002;47:3567–3578.
3. Merchant TE. MR spectroscopy of the breast. *Magn Reson Imaging Clin N Am* 1994;2:691–703.
4. Miller BL. A review of chemical issues in 1H NMR spectroscopy: N-acetyl-L-aspartate, creatine and choline. *NMR Biomed* 1991;4:47–52.
5. Miller BL, Chang L, Booth R, *et al.* In vivo 1H MRS choline: Correlation with in vitro chemistry/histology. *Life Sci* 1996; 58:1929–1935.
6. Kurhanewicz J, Vigneron DB, Hricak H, *et al.* Prostate cancer: Metabolic response to cryosurgery as detected with 3D H-1 MR spectroscopic imaging. *Radiology* 1996;200:489–496.
7. Kurhanewicz J, Vigneron DB, Hricak H, *et al.* Three-dimensional H-1 MR spectroscopic imaging of the in situ human prostate with high (0.24–0.7 cm^3) spatial resolution. *Radiology* 1996;198:795–805.
8. Heerschap A, Jager GJ, van der Graaf M, *et al.* In vivo proton MR spectroscopy reveals altered metabolite content in malignant prostate tissue. *Anticancer Res* 1997;17:1455–1460.
9. van Zijl PC, Moonen CT, Gillen J, *et al.* Proton magnetic resonance spectroscopy of small regions (1 mL) localized inside superficial human tumors. A clinical feasibility study. *NMR Biomed* 1990;3:227–232.
10. Roebuck JR, Cecil KM, Schnall MD, *et al.* Human breast lesions: Characterization with proton MR spectroscopy. *Radiology* 1998;209:269–275.
11. Mackinnon WB, Barry PA, Malycha PL, *et al.* Fine-needle biopsy specimens of benign breast lesions distinguished from invasive cancer ex vivo with proton MR spectroscopy. *Radiology* 1997;204:661–666.
12. Gribbestad IS, Singstad TE, Nilsen G, *et al.* In vivo 1H MRS of normal breast and breast tumors using a dedicated double breast coil. *J Magn Reson Imaging* 1998;8:1191–1197.
13. Star-Lack J, Vigneron DB, Pauly J, *et al.* Improved solvent suppression and increased spatial excitation bandwidths for three-dimensional PRESS CSI using phase-compensating spectral/spatial spin-echo pulses. *J Magn Reson Imaging* 1997;7:745–757.
14. Adalsteinsson E, Irarrazabal P, Topp S, *et al.* Volumetric spectroscopic imaging with spiral-based k-space trajectories. *Magn Reson Med* 1998;39:889–898.
15. Rabinov JD, Lee PL, Barker FG, *et al.* In vivo 3-T MR spectroscopy in the distinction of recurrent glioma versus radiation effects: Initial experience. *Radiology* 2002;225:871–879.
16. Dydak U, Weiger M, Pruessmann KP, *et al.* Sensitivity-encoded spectroscopic imaging. *Magn Reson Med* 2001;46: 713–722.
17. Wald LL, Moyher SE, Day MR, *et al.* Proton spectroscopic imaging of the human brain using phased array detectors. *Magn Reson Med* 1995;34:440–445.
18. Pirzkall A, McKnight TR, Graves EE, *et al.* MR-spectroscopy guided target delineation for high-grade gliomas. *Int J Radiat Oncol Biol Phys* 2001;50:915–928.
19. Kurhanewicz J, Vigneron DB, Nelson SJ. Three-dimensional magnetic resonance spectroscopic imaging of brain and prostate cancer. *Neoplasia (NY)* 2000;2:166–189.
20. Dowling C, Bollen AW, Noworolski SM, *et al.* Preoperative proton MR spectroscopic imaging of brain tumors: Correlation with histopathologic analysis of resection specimens [see comments]. *AJNR Am J Neuroradiol* 2001;22:604–612.
21. Nelson SJ, Graves E, Pirzkall A, *et al.* In vivo molecular imaging for planning radiation therapy of gliomas: An application of 1H MRSI. *J Magn Reson Imaging* 2002;16:464–476.
22. Negendank W. Studies of human tumors by MRS: A review. *NMR Biomed* 1992;5:303–324.
23. Alger JR, Frank JA, Bizzi A, *et al.* Metabolism of human gliomas: Assessment with H-1 MR spectroscopy and F-18 fluorodeoxyglucose PET [see comments]. *Radiology* 1990; 177:633–641.
24. Wald LL, Nelson SJ, Day MR, *et al.* Serial proton magnetic resonance spectroscopy imaging of glioblastoma multiforme after brachytherapy. *J Neurosurg* 1997;87:525–534.
25. Pirzkall A, Nelson SJ, McKnight TR, *et al.* Metabolic imaging of low-grade gliomas with three-dimensional magnetic resonance spectroscopy. *Int J Radiat Oncol Biol Phys* 2002;53: 1254–1264.
26. McKnight TR, von dem Bussche MH, Vigneron DB, *et al.* Histopathological validation of a three-dimensional magnetic resonance spectroscopy index as a predictor of tumor presence. *J Neurosurg* 2002;97:794–802.
27. Hunjan S, Harsh G, Gibbs I, *et al.* Validating magnetic resonance spectroscopic imaging for radiation therapy guidance [Abstract]. *Proc Am Soc Therap Radiol Oncol* 2002;54(Suppl. 2):29.
28. Frahm J, Bruhn H, Gyngell ML, *et al.* Localized proton NMR spectroscopy in different regions of the human brain in vivo. Relaxation times and concentrations of cerebral metabolites. *Magn Reson Med* 1989;11:47–63.
29. Michaelis T, Merboldt KD, Bruhn H, *et al.* Absolute concentrations of metabolites in the adult human brain in vivo: Quantification of localized proton MR spectra [Erratum appears in *Radiology* 1993;188:288]. *Radiology* 1993;187:219–227.
30. Pouwels PJ, Frahm J. Regional metabolite concentrations in human brain as determined by quantitative localized proton MRS. *Magn Reson Med* 1998;39:53–60.
31. Pfeuffer J, Tkac I, Provencher SW, *et al.* Toward an in vivo neurochemical profile: Quantification of 18 metabolites in short-echo-time (1)H NMR spectra of the rat brain. *J Magnet Resonance* 1999;141:104–120.
32. Bottomley PA. Spatial localization in NMR spectroscopy in vivo. *Ann N Y Acad Sci* 1987;508:333–348.
33. Drost DJ, Riddle WR, Clarke GD, *et al.* Proton magnetic resonance spectroscopy in the brain: Report of AAPM MR Task Group #9. *Med Phys* 2002;29:2177–2197.
34. Haase A, Frahm J, Hanicke W, *et al.* 1H NMR chemical shift selective (CHESS) imaging. *Phys Med Biol* 1985;30:341–344.
35. Spielman DM, Adalsteinsson E, Lim KO. Quantitative assessment of improved homogeneity using higher-order shims for spectroscopic imaging of the brain. *Magn Reson Med* 1998; 40:376–382.
36. Kim DH, Adalsteinsson E, Glover GH, *et al.* Regularized higher-order in vivo shimming. *Magn Reson Med* 2002;48: 715–722.
37. Jackson JI, Mayer CH, Nishimura DG, *et al.* Selection of a convolution function for fourier inversion using gridding. *IEEE Trans Med Imag* 1991;10:473–478.
38. McKnight TR, Noworolski SM, Vigneron DB, *et al.* An automated technique for the quantitative assessment of 3D-MRSI data from patients with glioma. *J Magn Reson Imaging* 2001;13:167–177.